

Magnetotransport in Topological Dirac Semimetal α -Sn

Owen Vail, Patrick Taylor, Patrick Folkes, Barbara Nichols, and George de Coster
US Army Research Laboratory, Adelphi, MD 20783, USA

(Dated: June 21, 2022)

We report the first magnetotransport evidence of Dirac semimetal behavior in α -Sn thin films grown on CdTe. Topological electronics represents a new paradigm of robust quantum states in condensed matter systems. The high spin orbit coupling in thin films of the zero-gap semiconductor α -Sn can cause nontrivial topology and Dirac semimetallic states in the material. An insulating substrate like CdTe is required to electrically isolate the film and fully exploit its electronic properties for practical device applications. We characterize epitaxial α -Sn growth on CdTe(111)B using noninvasive techniques to verify the film's high quality pseudomorphic growth. By overcoming ex-situ fabrication obstacles on uncapped films, we perform magnetotransport measurements in a Hall bar geometry and identify semimetallic behavior at low temperature. Subsequent analysis reveals three-carrier transport with quantum oscillations indicating a non-trivial Berry phase.

I. INTRODUCTION

The diamond-cubic phase of tin (Sn), known as α -Sn, has long been of experimental and theoretical interest due to its inverted electronic bulk band structure [1, 2]. Such an inversion in a elemental material makes α -Sn singularly exciting to investigate as a topological material because the strong spin orbit coupling required to cause a topological band inversion generally limits the choice of materials for study to complex compounds or heterostructures such as an engineered quantum well, ternary or quaternary compounds, or use of poisonous elements like mercury [3–9]. However, spin orbit coupling strength can be increased even in single element crystals by picking heavier constituent elements. As an example, graphene is effectively a single element 2D Dirac semimetal (DSM) due to its low spin orbit coupling [10]. Replacing the carbon atoms in the honeycomb lattice with their heavier counterpart of Sn creates stanene which is a two-dimensional topological insulator with a large inverted band gap and well defined edge states [11, 12].

Replacing carbon atoms in a three dimensional diamond cubic lattice with Sn can also achieve non-trivial topological physics. Indeed, through different strain, orientation, and thickness configurations one can achieve two and three dimensional topological insulator and DSM states in α -Sn thin films [14–16]. The ability to produce and process high quality Sn films will be a significant boon in achieving the diverse applications of topological physics such as efficient nonvolatile memory and low voltage devices [17–20]. The persistence of the topological states near room temperature could enable these applications to be employed in all manner of environments [21–23].

The diamond cubic α -Sn phase is generally stable below 13.2°C, otherwise it undergoes a structural transition to the β -Sn phase. The critical temperature of this phase transition can be pushed above room temperature when the α -Sn is grown in thin films by molecular beam epitaxy (MBE) due to the stabilizing effect of a diamond

cubic substrate [24]. Unlike the metallic β -Sn phase, unstrained bulk α -Sn is a zero-gap semiconductor. Tensile epitaxial strain and thickness dependent quantum confinement can create band gaps in thin films that are large enough to limit thermal excitations even at room temperature [3, 25], while compressive strain can cause sufficiently thick films to be DSMs [4]. The various topological phases achievable in Sn structures critically depend on the spin orbit coupling and mass Darwin effect induced band inversion between the Γ_8^+ and Γ_7^- bands, revealing nontrivial topology in transport measurements when the Fermi level is positioned appropriately [2]. We remark that α -Sn can be thought of as the inversion symmetric case of HgTe, which hosts many of the same topological states predicted in α -Sn. However, unlike α -Sn, compressive epitaxial strain does not yield a DSM state in HgTe due to its broken inversion symmetry [26].

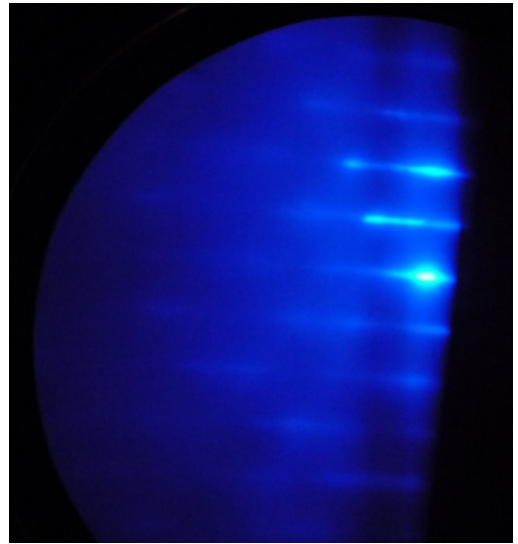


FIG. 1. RHEED pattern observed during the MBE α -Sn growth of α -Sn along a $\langle 110 \rangle$ azimuth provides evidence for coherent epitaxial alignment with CdTe(111)B and smooth surface morphology.

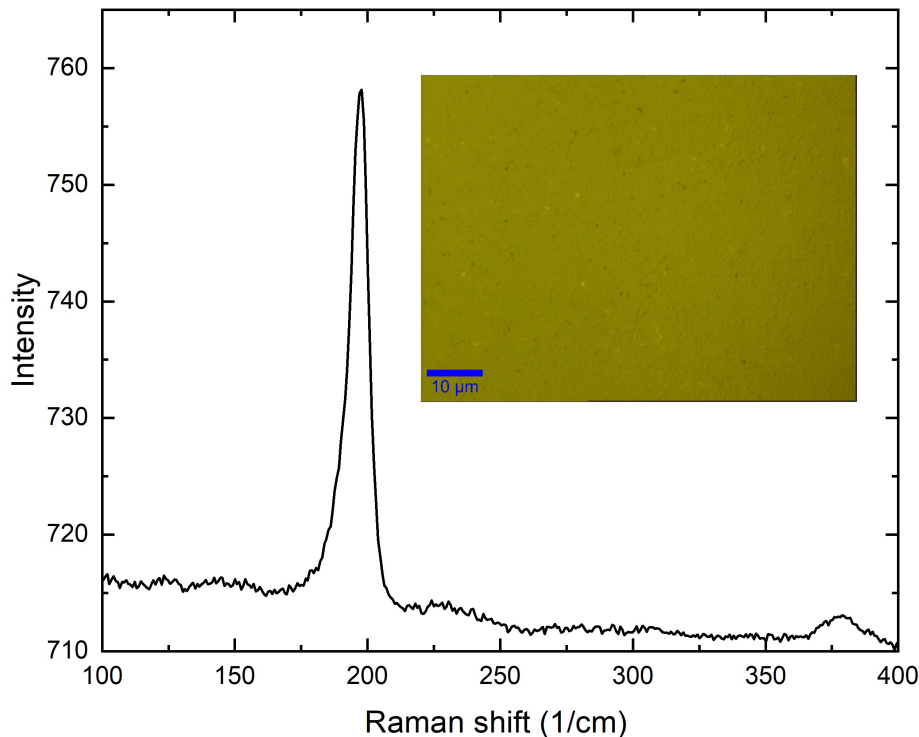


FIG. 2. Raman spectroscopy and optical inset of α -Sn thin film. The 1Γ peak in intensity at 198 cm^{-1} is characteristic of the diamond cubic phase of Sn. Combined with the observed smooth morphology (inset), this indicates a high quality film growth. An additional peak near 379 cm^{-1} and background between 200 and 350 cm^{-1} are consistent with the two phonon overtones in α -Sn(111) [13].

An insulating substrate is of critical importance to the electronic application of thin film topological materials. The zincblende crystal structure of CdTe has a lattice constant ($a = 6.481 \text{ \AA}$) well matched to α -Sn ($a = 6.4892 \text{ \AA}$), and is insulating with a 1.6 eV band gap [27, 28]. The (111) projection of the diamond-cubic lattice is particularly exciting because it is honeycomb, such that pseudomorphic monolayer growth on this surface may yield stanene. By epitaxially growing α -Sn on CdTe(111) and tuning the film thickness, it may be possible to observe a variety of quantum confinement induced topological states, including monolayer stanene. Fundamental growth and fabrication techniques are lacking for the α -Sn/CdTe material system when compared with its InSb counterpart. However, the narrow band gap of InSb imposes parallel transport channels to the α -Sn making it ill-suited for device engineering. Transport devices fabricated from α -Sn/CdTe heterostructures give insight into its promise as a practical electronic platform.

II. METHODS

Substrates of Te terminated CdTe(111)B surfaces were selected for α -Sn growth, as the Te atoms bond covalently with Sn, enforcing the diamond lattice formation of α -Sn formation. Growth of α -Sn on the Cd terminated CdTe(111)A has been found to be rougher due to the metallic bonding between Sn and Cd atoms. The CdTe surface is treated with a bromine etch to attain a Te-rich layer that will thermally desorb during annealing. The

substrate is annealed in 10^{-10} Torr at 250 - $300 \text{ }^\circ\text{C}$, and Reflection High-Energy Electron Diffraction (RHEED) oscillations are taken to characterize the pristine (111)B surface. In order to promote the formation of an abrupt interface, the substrate is allowed to cool in vacuum to a temperature of $-15 \text{ }^\circ\text{C}$ before α -Sn is grown through the beaming of Sn molecules onto the cold hexagonal surface. RHEED oscillations taken during MBE growth indicate a well-ordered crystal formation along a $\langle 110 \rangle$ azimuth (Fig. 1). A strong RHEED pattern indicates coherent epitaxial alignment with the CdTe(111)B substrate and correlates with smooth surface morphology.

After the films are removed from vacuum, Raman spectroscopy is performed using a Witech alpha300A microscope and a 532 nm wavelength laser operating at room temperature with 1 mW beam power in a $1 \mu\text{m}$ spot size and a 10 s measurement time to avoid heating of the sample. We identify the α -Sn 1Γ peak at 198 cm^{-1} (Fig. 1) [29] and observe the surface morphology in order to confirm high quality α -Sn growth. The α -Sn Raman peak is still prevalent after months of exposure without a capping layer, which bodes well for ex-situ processing and realistic applications that cannot be done under vacuum. By increasing the beam intensity over 50 mW, we are able to cause local transitions to β -Sn optically visible as patches of white on a grey Sn surface with no Raman peak near 198 cm^{-1} .

While shifts in the Raman spectrum give some indication of epitaxially compressive strain in the film [30], X-ray diffraction (XRD) provides more detailed information with respect to the α -Sn diamond-cubic crystal

III. EXPERIMENT

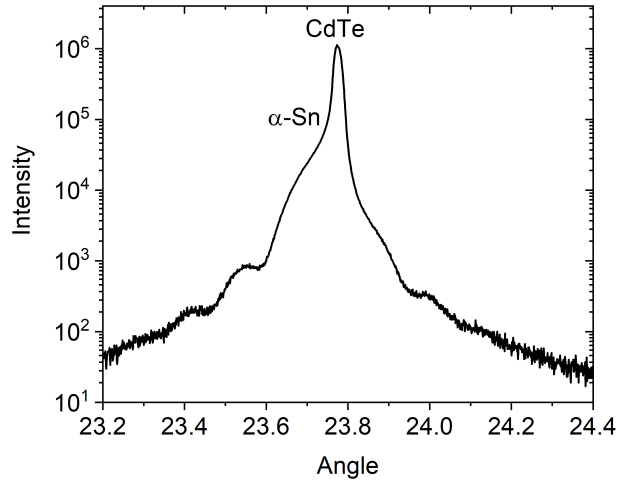


FIG. 3. θ - 2θ XRD spectra of α -Sn grown on a CdTe(111) substrate. The minimal shift between α -Sn and CdTe peaks implies pseudomorphic growth with compressive strain. Kiessig fringes appear symmetrically around the α -Sn peak.

structure on the CdTe substrate. Fig 3 shows the symmetric θ - 2θ (111) X-ray reflection from this sample. The main peak is a convolution of signals from the CdTe(111) and α -Sn(111), with the CdTe being responsible for the mammoth peak and the α -Sn arising as a shoulder on the left-hand side. The position of these peaks implies pseudomorphic crystal growth with a lattice constant for the α -Sn film which exceeds that of the CdTe substrate. If we assume the unit cell volume is conserved, the lattice distortion is consistent with compressive strain in the film causing Poisson expansion in the growth direction. Kiessig fringes appear as symmetric ripples about the α -Sn peak [31]. These fringes give information about the thickness of the layer, which we approximate as 45 nm. Though this is not an exact measurement of thickness, it is in agreement with the estimated 48 nm thickness extrapolated from growth rates. According to convention, a bilayer of α -Sn(111) is defined as a single layer of stanene, which is a buckled honeycomb lattice of Sn atoms. The distance between bilayers is 3.748 Å, implying a thin film thickness of approximately 120 bilayers.

Thin films of α -Sn have been shown to transition to β -Sn at temperatures near 70°C [32]. With this in mind, a room temperature vacuum anneal is used to cure polymer for lithographic device design. Dry etching of Hall bars using argon plasma affords precision and abrupt mesa sidewalls. The resulting mesoscopic ($20 \times 10 \mu\text{m}^2$) Hall bars are contacted using electron beam evaporation. As the CdTe substrate is particularly brittle, a chrome adhesion layer and ball bonding technique helps guarantee the success of subsequent device bonding. The resulting packaged devices resemble end-user electronics that can be plugged in like a computer chip.

Achieving an abrupt CdTe/ α -Sn interface can be particularly difficult [33] especially when compared with a substrate like InSb [4]. Furthermore, the irregularity of the surface quality of industrially purchased material greatly affects the reproducibility of high-quality α -Sn films. However, the low carrier density of the semi-insulating substrate (less than 10^{12} cm^{-3} with 10^{14} cm^{-3} dopant density) allows for a simplified model of the conduction pathways in the system by assuming that the contribution of the substrate to the transport properties is negligible. With this in mind, Hall bars fabricated on samples of α -Sn on CdTe are studied in a liquid helium cryostat under application of a perpendicular magnetic field.

While the film thickness extrapolated from the growth rate for this sample is 48 nm, a layer of stannous oxide is expected to form from the topmost layers of Sn atoms due to atmospheric oxidation, resulting in a film thickness of approximately 46 nm [34], which we will use in subsequent calculations. This is far thicker than the thin films in recent transport studies of α -Sn [35] and we should expect a 46 nm thick α -Sn film grown on CdTe(111)B to be a DSM according to theoretical calculations and high resolution electron energy loss spectroscopy measurements of thin film α -Sn band structures [14, 15, 36].

A. Temperature Dependence of the Longitudinal Resistance

By applying 10 μA of direct current and measuring the longitudinal resistance of the Hall bar using a 4-point setup, the linear current-voltage curve is found to pass through the origin with $\pm 0.1 \Omega$ of accuracy and stability. As the temperature of the device is reduced, the resistance initially increases exponentially with temperature, similar to the behavior of a semiconductor [37]. Using a combination of liquid nitrogen and liquid helium measurements, we establish a full temperature range with two distinct regimes, one with metallic behavior and one semiconducting (Fig. 4). We use an Arrhenius model for the semiconducting resistance R_{semi} near room temperature with thermal carriers excited across a gap:

$$R_{\text{semi}}(T) = R_{\infty} e^{\frac{E_g}{k_B T}}, \quad (1)$$

where k_B is the Boltzmann constant, R_{∞} is the resistance at high temperature, and E_g is the thermal activation energy.

We can also understand the metallic channel resistance $R_{\text{metal}}(T)$ through the Bloch-Grüneisen model for the resistance of electrons interacting with phonons in a metal [38]:

$$\frac{1}{R_{\text{metal}}(T) - R_0} = \frac{1}{C_1 T^5} + \frac{1}{C_2 T}. \quad (2)$$

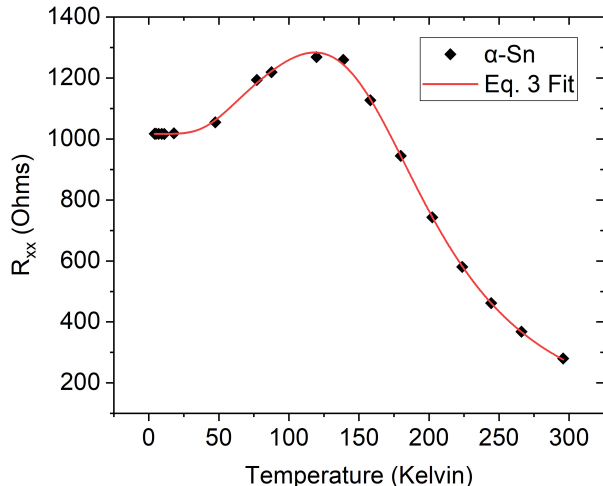


FIG. 4. Temperature dependence of α -Sn device resistance on CdTe(111)B. The device exhibits semiconducting behavior near room temperature and metallic behavior at lower temperatures. There is good agreement between the full curve and Eq. (3), with a thermal activation energy of 81 meV.

Here C_1 and C_2 are related to the prevalence of electron-phonon interactions in the metallic channel and the geometry of the Hall bar, and R_0 is the resistance at $T = 0$ due to electron-defect scattering. The T^5 scaling of the first term in Eq. (2) corresponds to the low temperature resistivity of a three dimensional metal (or a doped DSM [39–41]), while a two dimensional metal would have a T^4 scaling [42]. As the best fit uses a T^5 scaling and minimizes any T^4 component, we conclude that the dominant transport channel is three dimensional. This is consistent with the topological surface state of DSM α -Sn being buried in the bulk valence and sub-valence bands [25].

If we assume a thin metallic channel in parallel with the semiconducting one, the total resistance is given by

$$\frac{1}{R(T)} = \frac{1}{R_{\text{semi}}(T)} + \frac{1}{R_{\text{metal}}(T)}, \quad (3)$$

By fitting the full temperature range with Eq. (3), we find $C_1 = 2.84 \times 10^{-7} \Omega/\text{K}^5$, $C_2 = 2.77 \Omega/\text{K}$, $R_0 = 1017 \Omega$, and $R_\infty = 13.6 \Omega$, and extract a $E_g = 81$ meV thermal excitation energy. This activation gap obtained for the semiconducting region falls within accepted values of the $L_{6c}^+ - \Gamma_{8vc}^+$ indirect band gap of unstrained α -Sn [43], suggesting that indirect interband transitions are responsible for the semiconducting behavior. Previous studies on α -Sn found a significant temperature dependence to this gap [44] but attempts to include this parameter in Eq. (1) do not affect the other parameters and the magnitude of temperature dependence is minimized, resembling the results found by Lavine and Ewald [45] at low temperature. The best fit reveals a reduction in E_g of only 5 meV at room temperature. We can expect the epitaxial strain to play a significant role in the indirect

band gap [44], especially at these thin film thicknesses, and may be a potential source of deviation from previous reports. In summation, we find the behavior of $R(T)$ in Eq. (3) to be dominated by $R_{\text{semi}}(T)$ near room temperature and $R_{\text{metal}}(T)$ near and below 70K, implying that studies of the metallic behavior may be accessible at liquid nitrogen temperatures. We should expect the low temperature transport properties of thin film DSMs to be metallic in nature, dominated by intraband scattering mechanisms [39, 40]. In fact, the high temperature crossover to semiconductor-like transport is consistent with the R-T curves measured in other thin film DSMs such as Na_3Bi and Cd_3As_2 [46–49].

B. Magnetic Field Dependence of the Longitudinal and Hall Resistances

At low temperature, the device reached a finite resistance that no longer depended on temperature. Upon application of a low magnetic field in the 0.1 Tesla (T) range, the Hall resistance (R_{xy}) increased, consistent with an electron-like charge carrier. The longitudinal resistance (R_{xx}) exhibited a quadratic dependence, which is common for materials with multiple carriers [37]. We find that the full range (up to 9 T) of R_{xx} and R_{xy} data is best fit simultaneously by a three carrier model. This does not impose an upper limit on the number of carrier channels as other carriers with similar mobilities to those used would simply add to (or subtract from) the relevant carrier density, but it does provide insight into the carrier dynamics in the material. The longitudinal and transverse resistivities are found by inverting the three-carrier conductivity tensor:

$$\begin{aligned} \sigma_{xx} &= \frac{n_1 e \mu_1}{1 + (\mu_1 B)^2} + \frac{n_2 e \mu_2}{1 + (\mu_2 B)^2} + \frac{n_3 e \mu_3}{1 + (\mu_3 B)^2}, \\ \sigma_{xy} &= \frac{n_1 e \mu_1^2 B}{1 + (\mu_1 B)^2} + \frac{n_2 e \mu_2^2 B}{1 + (\mu_2 B)^2} + \frac{n_3 e \mu_3^2 B}{1 + (\mu_3 B)^2}, \\ \rho_{xx} &= \frac{\sigma_{xx}}{\sigma_{xx}^2 + \sigma_{xy}^2}, \quad \rho_{xy} = \frac{\sigma_{xy}}{\sigma_{xx}^2 + \sigma_{xy}^2}. \end{aligned} \quad (4)$$

Here e is the electron charge, B is the applied field, n_1 , n_2 , and n_3 are carrier densities, and μ_1 , μ_2 , and μ_3 are carrier mobilities. We have defined the sign of these quantities to be positive for n-type carriers and negative for p-type carriers. Three dimensional resistances are found from these quantities using the geometry of the Hall bar ($\rho = R \times 23 \square\text{nm}$). The resulting fit (Fig. 5) gives electron-like and hole-like carriers with similar

$\mu_1 = 4100 \text{ cm}^2/\text{Vs}$	$n_1 = 3.18 \times 10^{17} \text{ cm}^{-3}$
$\mu_2 = -2520 \text{ cm}^2/\text{Vs}$	$n_2 = -2.41 \times 10^{17} \text{ cm}^{-3}$
$\mu_3 = -40 \text{ cm}^2/\text{Vs}$	$n_3 = -1.75 \times 10^{19} \text{ cm}^{-3}$

TABLE I. Table of magnetoresistance carrier concentrations and mobilities.

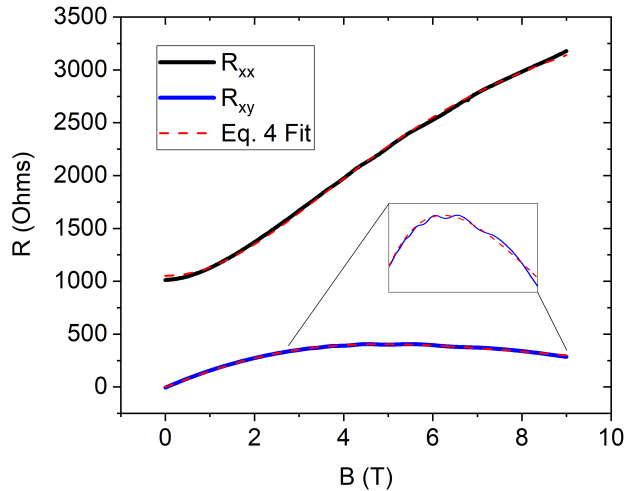


FIG. 5. Magnetic field dependence of the longitudinal and transverse resistance at 4.2 K for an α -Sn thin film grown on CdTe(111)B. The nonlinear behavior of R_{xx} and R_{xy} is expected in real metals and semimetals, and indicates three carrier channels. The curves are fit with Eq. (4) in order to extract the carrier densities and mobilities. Inset is a rescaling of R_{xy} in order to clarify the presence of quantum oscillations.

carrier densities and a bulk hole-like carrier with significantly reduced mobility found in Table I. The value of n-type carrier density and mobility is consistent with earlier studies of α -Sn crystals [45, 50].

Under a strong magnetic field (> 2.5 T) Shubnikov de-Haas (SdH) oscillations were observed. Background polynomials are subtracted from R_{xx} and R_{xy} , giving ΔR_{xx} and ΔR_{xy} , such that the periodic oscillations can be clearly seen as a function of $1/B$ (Fig 6). Confirming peak-to-peak measurements with a Fourier transform reveals an oscillation period of $B_0 = 21.56$ T. If we assume an isotropic Fermi surface in a three dimensional semimetal at low temperature, we can calculate a SdH carrier density n_{SdH} using:

$$n_{SdH} = 2 \frac{4\pi}{3} \frac{k_F^3}{(2\pi)^3} = \frac{1}{3\pi^2} \left(\frac{2eB_0}{\hbar} \right)^{3/2}, \quad (5)$$

where E_F is the Fermi energy, ω_c is the cyclotron frequency, and \hbar is the reduced plank constant. The resulting carrier density is $n_{SdH} = 5.66 \times 10^{17} \text{ cm}^{-3}$. This carrier density and the mobility implied by the onset of SdH oscillations ($4000 \text{ cm}^2/\text{Vs}$) are consistent with the electron-like carrier found by Hall analysis. A more realistic calculation of the carrier density, factoring in the anisotropy of the Fermi surface in the k_z direction, would be expected to improve the agreement between the two analyses [15].

SdH oscillations are a consequence of Landau quantization of low carrier density states. Sequential emptying of Landau levels (LLs) leads to oscillations in the conductivity, such that minimas in σ_{xx} correspond to integer

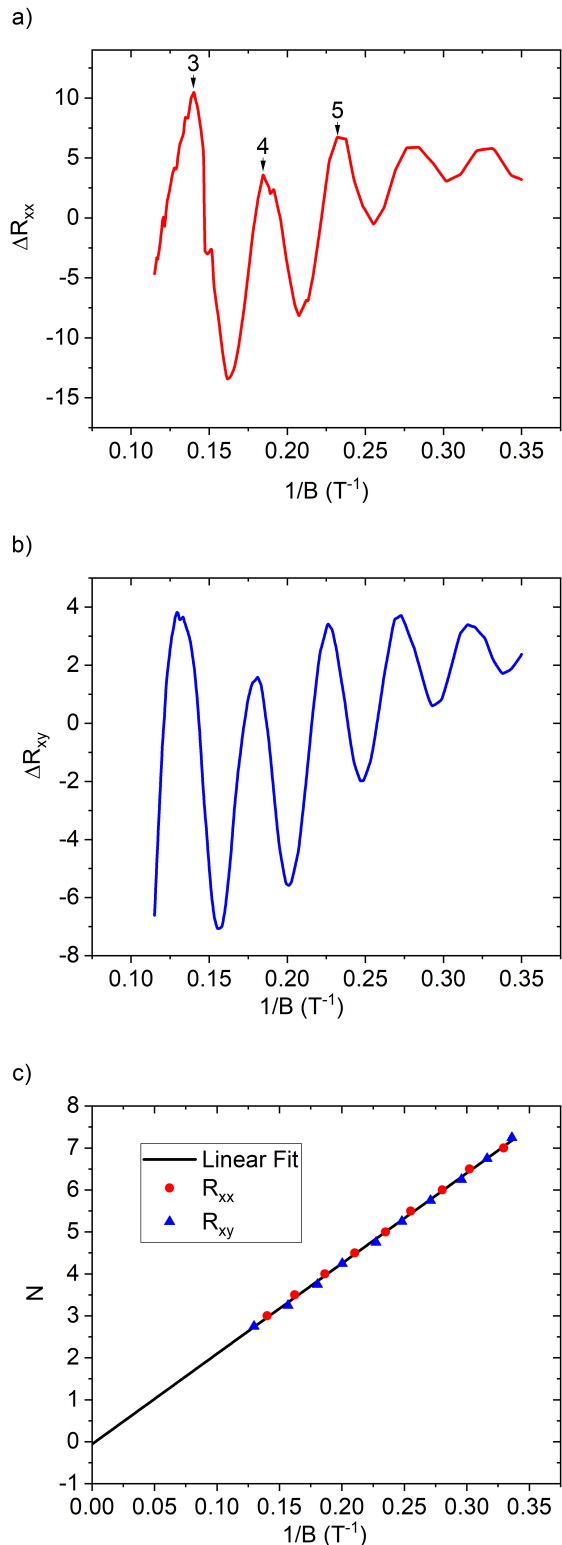


FIG. 6. High magnetic field Shubnikov de-Haas oscillations of a) ΔR_{xx} and b) ΔR_{xy} . Extrema are assigned to their corresponding fractional LLs and used to construct a linear fit c) with a slope of 21.56 T and an intercept of -0.063 . This intercept provides direct evidence of Dirac dispersion via Eq. (5).

LLs. By noting $\rho_{xx} \gg \rho_{xy}$ at all fields, this implies that $\sigma_{xx} \gg \sigma_{xy}$ and $\rho_{xx} \sim 1/\sigma_{xx}$ by Eq. (4). Therefore the maxima of ΔR_{xx} are assigned to integer LL indices (N), while minima are assigned to half integers [51]. Extrema of ΔR_{xy} are phase-shifted by 1/4 [35, 51], and thereby correspond to quarter integer Landau levels (N+1/4 for the minima and N+3/4 for the maxima of the transverse resistance). Analyzing just the oscillatory argument of the Lifshitz-Kosevich theory [52, 53], resulting from the Lifshitz-Onsager quantization rule [54], we fit the Landau level index with

$$N = B_0/B + \gamma - \delta, \quad (6)$$

$\delta = 1/8$ is a phase shift determined by the dimensionality corresponding to electron-like carriers in a 3D metal. γ is the topologically relevant parameter, with

$$|\gamma - \delta| = \left| \frac{1}{2} - \frac{\phi_B}{2\pi} - \delta \right|, \quad (7)$$

where ϕ_B is the Berry phase [55]. As such, $\gamma = \frac{1}{2}$ would correspond to a trivial Schrödinger state whereas $\gamma = 0$ reveals a Dirac state with $\phi_B = \pi$. We find $\gamma = 0.062$, indicating that the dominant electron-like channel corresponds to a 3D Dirac semimetal.

The coexistence of both electron and hole-like carriers in a semimetal can be attributed to several potential mechanisms. For example, any finite temperature in a DSM with a Fermi level at the Dirac point will induce hole and electron populations due to the gapless nature of Dirac cones. Additionally, topological surface states, tilt of the Dirac cones, or defect states near the charge neutrality point could play a role in determining $n_{1/2}$ and $\mu_{1/2}$ [56]. n_3 is a parallel bulk conduction channel that may come from the heavy hole Γ_8^+ valence band.

IV. CONCLUSION

In conclusion, we epitaxially grew and characterized 3D DSM α -Sn on CdTe(111)B. Non-invasive techniques were used to verify the high quality pseudomorphic growth of the film, followed by direct transport measurement. Films were found to have semiconducting behavior at room temperature and metallic behavior at low temperature with three carrier types. The π Berry phase of the DSM state was unambiguously characterized by extrapolating the observed SdH oscillations to the zero-energy Landau level. By surmounting the challenges associated with growth and fabrication of single element α -Sn thin film devices on insulating CdTe, we provide a platform for future topological electronics based on this heterostructure. Moreover, the results presented indicate that capping and single digit Kelvin temperatures may be unnecessary to access the DSM regime of α -Sn, opening the doors to a host of practical device applications. By reducing the thickness of MBE grown α -Sn and introducing quantum confinement, we hope to access a wide array of topological device engineering. As such, further transport studies on samples of this nature will help identify the best route toward a single-element topological system that is functional in the field.

ACKNOWLEDGMENTS

This research was partially supported by a Laboratory University Collaborative Initiative award provided by the Basic Research Office in the Office of the Under Secretary of Defense for Research and Engineering.

-
- [1] S. Groves and W. Paul, Phys. Rev. Lett. **11**, 194 (1963).
 - [2] S. Küfner and F. Bechstedt, Phys. Rev. B **91**, 035311 (2015).
 - [3] A. Barfuss, L. Dudy, M. R. Scholz, H. Roth, P. Höpfner, C. Blumenstein, G. Landolt, J. H. Dil, N. C. Plumb, M. Radovic, et al., Phys. Rev. Lett. **111**, 157205 (2013).
 - [4] C.-Z. Xu, Y.-H. Chan, Y. Chen, P. Chen, X. Wang, C. Dejoie, M.-H. Wong, J. A. Hlevyack, H. Ryu, H.-Y. Kee, et al., Phys. Rev. Lett. **118**, 146402 (2017).
 - [5] M. Z. Hasan and C. L. Kane, Reviews of Modern Physics **82**, 3045 (2010).
 - [6] M. Franz and L. Molenkamp, *Topological Insulators, Volume 6 (Contemporary Concepts of Condensed Matter Science)* (Elsevier, 2013), ISBN 0444633146.
 - [7] B. A. Bernevig, T. L. Hughes, and S.-C. Zhang, Science **1757**, 1 (2006).
 - [8] L. Fu and C. L. Kane, Phys. Rev. B **76**, 045302 (2007).
 - [9] L. Fu, Phys. Rev. Lett. **106**, 106802 (2011).
 - [10] C. L. Kane and E. J. Mele, Phys. Rev. Lett. **95**, 226801 (2005).
 - [11] Y. Xu, B. Yan, H.-J. Zhang, J. Wang, G. Xu, P. Tang, W. Duan, and S.-C. Zhang, Phys. Rev. Lett. **111**, 136804 (2013).
 - [12] C.-Z. Xu, Y.-H. Chan, P. Chen, X. Wang, D. Flötto, J. A. Hlevyack, G. Bian, S.-K. Mo, M.-Y. Chou, and T.-C. Chiang, Phys. Rev. B **97**, 035122 (2018).
 - [13] M. Iliev, M. Sinyukov, and M. Cardona, Phys. Rev. B **16**, 5350 (1977).
 - [14] G. J. de Coster, P. A. Folkes, P. J. Taylor, and O. A. Vail, Phys. Rev. B **98**, 115153 (2018).
 - [15] H. Huang and F. Liu, Phys. Rev. B **95**, 201101 (2017).
 - [16] A. A. Abrikosov and S. D. Beneslavskii, Zh. Eksp. Teor. Fiz. **59**, 1280 (1971), [Sov. Phys. JETP **32**, 669, (1971)].
 - [17] X. Li, Y. G. Semenov, and K. W. Kim, Applied Physics Letters **104**, 061116 (2014).
 - [18] Y. G. Semenov, X. Duan, and K. W. Kim, Phys. Rev. B **86**, 161406 (2012).
 - [19] Y. G. Semenov, X. Duan, and K. W. Kim, Phys. Rev. B **89**, 201405 (2014).

- [20] A. R. Mellnik, J. S. Lee, A. Richardella, J. L. Grab, P. J. Mintun, M. H. Fischer, A. Vaezi, A. Manchon, E.-A. Kim, N. Samarth, et al., *Nature* **511**, 449 (2014).
- [21] J.-C. Rojas-Sánchez, S. Oyarzún, Y. Fu, A. Marty, C. Vergnaud, S. Gambarelli, L. Vila, M. Jamet, Y. Ohtsubo, A. Taleb-Ibrahimi, et al., *Phys. Rev. Lett.* **116**, 096602 (2016).
- [22] C. H. Li, O. M. J. van 't Erve, J. T. Robinson, Y. Liu, L. Li, and B. T. Jonker, *Nature Nanotechnology* **9**, 218 (2014).
- [23] Y. Ohtsubo, P. Le Fèvre, F. Bertran, and A. Taleb-Ibrahimi, *Phys. Rev. Lett.* **111**, 216401 (2013).
- [24] R. Farrow, D. Robertson, G. Williams, A. Cullis, G. Jones, I. Young, and P. Dennis, *Journal of Crystal Growth* **54**, 507 (1981), ISSN 0022-0248.
- [25] V. A. Rogalev, T. Rauch, M. R. Scholz, F. Reis, L. Dudy, A. Fleszar, M.-A. Husanu, V. N. Strocov, J. Henk, I. Mertig, et al., *Phys. Rev. B* **95**, 161117 (2017).
- [26] S. Zaheer, S. M. Young, D. Cellucci, J. C. Y. Teo, C. L. Kane, E. J. Mele, and A. M. Rappe, *Phys. Rev. B* **87**, 045202 (2013).
- [27] S. Adachi, *Properties of Group-IV, III-V and II-VI Semiconductors* (Wiley, 2005).
- [28] E. G. Novik, A. Pfeuffer-Jeschke, T. Jungwirth, V. Latussek, C. R. Becker, G. Landwehr, H. Buhmann, and L. W. Molenkamp, *Phys. Rev. B* **72**, 035321 (2005).
- [29] C. J. Buchenauer, M. Cardona, and F. H. Pollak, *Phys. Rev. B* **3**, 1243 (1971).
- [30] M. I. Bell, *physica status solidi (b)* **53**, 675 (1972).
- [31] H. Kiessig, *Naturwissenschaften* **18**, 847 (1930), ISSN 1432-1904.
- [32] J. Menéndez and H. Höchst, *Thin Solid Films* **111**, 375 (1984), ISSN 0040-6090.
- [33] H. Zimmermann, R. C. Keller, P. Meisen, and M. Seelmann-Eggebert, *Surface Science* **377-379**, 904 (1997).
- [34] F. Salt and J. Thomas, *Nature* **178**, 434 (1956).
- [35] Q. Barbedienne, J. Varignon, N. Reyren, A. Marty, C. Vergnaud, M. Jamet, C. Gomez-Carbonell, A. Lemaître, P. Le Fèvre, F. m. c. Bertran, et al., *Phys. Rev. B* **98**, 195445 (2018).
- [36] S. Takatani and Y. W. Chung, *Phys. Rev. B* **31**, 2290 (1985).
- [37] N. W. Ashcroft and N. D. Mermin, *Solid State Physics* (Cengage Learning, 1976), ISBN 0030839939.
- [38] J. M. Ziman, *Electrons and Phonons: The Theory of Transport Phenomena in Solids (Oxford Classic Texts in the Physical Sciences)* (Oxford University Press, 2001), ISBN 0198507798.
- [39] S. Das Sarma, E. H. Hwang, and H. Min, *Phys. Rev. B* **91**, 035201 (2015).
- [40] Y. I. Rodionov and S. V. Syzranov, *Phys. Rev. B* **91**, 195107 (2015).
- [41] F. Bloch, *Zeitschrift für Physik* **59**, 208 (1930), ISSN 0044-3328.
- [42] E. H. Hwang and S. Das Sarma, *Phys. Rev. B* **77**, 115449 (2008).
- [43] T. Brudevoll, D. S. Citrin, M. Cardona, and N. E. Christensen, *Phys. Rev. B* **48**, 8629 (1993).
- [44] C. A. Hoffman, J. R. Meyer, R. J. Wagner, F. J. Bartoli, M. A. Engelhardt, and H. Höchst, *Phys. Rev. B* **40**, 11693 (1989).
- [45] C. F. Lavine and A. Ewald, *J. Phys. Chem. Solids* **32**, 1121 (1971), ISSN 0022-3697.
- [46] C. Liu, J. Hellerstedt, M. T. Edmonds, and M. S. Fuhrer, *Phys. Rev. B* **96**, 235412 (2017).
- [47] Y. Zhou, J. Wu, W. Ning, N. Li, Y. Du, X. Chen, R. Zhang, Z. Chi, X. Wang, X. Zhu, et al., *Proceedings of the National Academy of Sciences* **113**, 2904 (2016), ISSN 0027-8424.
- [48] C.-Z. Li, L.-X. Wang, H. Liu, J. Wang, Z.-M. Liao, and D.-P. Yu, *Nature Communications* **6**, 10137 (2015).
- [49] C.-Z. Li, J.-G. Li, L.-X. Wang, L. Zhang, J.-M. Zhang, D. Yu, and Z.-M. Liao, *ACS Nano* **10**, 6020 (2016), PMID: 27166504.
- [50] J. G. Broerman, *Phys. Rev. Lett.* **24**, 450 (1970).
- [51] J. Xiong, Y. Luo, Y. H. Khoo, S. Jia, R. J. Cava, and N. P. Ong, *Phys. Rev. B* **86**, 045314 (2012).
- [52] X. Xiao, S. A. Yang, Z. Liu, H. Li, and G. Zhou, *Scientific Reports* **5**, 1 (2015).
- [53] A. R. Wright and R. H. McKenzie, *Phys. Rev. B* **87**, 085411 (2013).
- [54] D. Shoenberg, *Magnetic Oscillations in Metals*, Cambridge Monographs on Physics (Cambridge University Press, 1984).
- [55] H. Murakawa, M. S. Bahramy, M. Tokunaga, Y. Kohama, C. Bell, Y. Kaneko, N. Nagaosa, H. Y. Hwang, and Y. Tokura, *Science* **342**, 1490 (2013), ISSN 0036-8075.
- [56] A. A. Soluyanov, D. Gresch, Z. Wang, Q. Wu, M. Troyer, X. Dai, and B. A. Bernevig, *Nature* **527**, 495 (2015).